Cerebral Cortex, June 2018;28: 2192–2206

doi: 10.1093/cercor/bhy058
Advance Access Publication Date: 13 April 2018
Original Article

ORIGINAL ARTICLE

Altered Neocortical Gene Expression, Brain Overgrowth and Functional Over-Connectivity in *Chd8* Haploinsufficient Mice

Philipp Suetterlin[1,†], Shaun Hurley[1,†], Conor Mohan[1,†], Kimberley L. H. Riegman[1,†], Marco Pagani[2], Angela Caruso[3], Jacob Ellegood[4], Alberto Galbusera[2], Ivan Crespo-Enriquez[1], Caterina Michetti[5], Yohan Yee[4], Robert Ellingford[1], Olivier Brock[6], Alessio Delogu[6], Philippa Francis-West[1], Jason P. Lerch[4], Maria Luisa Scattoni[3], Alessandro Gozzi[2], Cathy Fernandes[7,8] and M. Albert Basson[1,8]

[1]Centre for Craniofacial and Regenerative Biology, King's College London, London SE1 9RT, UK, [2]Functional Neuroimaging Laboratory, Center for Neuroscience and Cognitive Systems @ UniTn, 38068 Rovereto, TN, Italy, [3]Research Coordination and Support Service, Istituto Superiore di Sanità, 00161 Rome, Italy, [4]Department of Medical Biophysics, University of Toronto, Mouse Imaging Centre, Hospital for Sick Children, Toronto, Ontario, Canada M5T 3H7, [5]Center for Synaptic Neuroscience and Technology, Istituto Italiano di Tecnologia, 16132 Genova, Italy, [6]Department of Basic and Clinical Neuroscience, Institute of Psychiatry, Psychology & Neuroscience, King's College London, London SE5 9NU, UK, [7]MRC Social, Genetic & Developmental Psychiatry Centre, PO82, Institute of Psychiatry, Psychology & Neuroscience, King's College London, De Crespigny Park, London SE5 8AF, UK and [8]MRC Centre for Neurodevelopmental Disorders, King's College London, London SE1 1UL, UK

Address correspondence to Dr M. Albert Basson, Centre for Craniofacial and Regenerative Biology, King's College London, Floor 27, Guy's Hospital Tower Wing, London SE1 9RT, UK. Email: albert.basson@kcl.ac.uk

[†]First co-authors.

Abstract

Truncating *CHD8* mutations are amongst the highest confidence risk factors for autism spectrum disorder (ASD) identified to date. Here, we report that *Chd8* heterozygous mice display increased brain size, motor delay, hypertelorism, pronounced hypoactivity, and anomalous responses to social stimuli. Whereas gene expression in the neocortex is only mildly affected at midgestation, over 600 genes are differentially expressed in the early postnatal neocortex. Genes involved in cell adhesion and axon guidance are particularly prominent amongst the downregulated transcripts. Resting-state functional MRI identified increased synchronized activity in cortico-hippocampal and auditory-parietal networks in *Chd8* heterozygous mutant mice, implicating altered connectivity as a potential mechanism underlying the behavioral phenotypes. Together, these data suggest that altered brain growth and diminished expression of important neurodevelopmental genes that

regulate long-range brain wiring are followed by distinctive anomalies in functional brain connectivity in *Chd8*$^{+/-}$ mice. Human imaging studies have reported altered functional connectivity in ASD patients, with long-range under-connectivity seemingly more frequent. Our data suggest that *CHD8* haploinsufficiency represents a specific subtype of ASD where neuropsychiatric symptoms are underpinned by long-range over-connectivity.

Key words: ASD, autism, axon guidance, behavior, CHD8, chromatin remodelling, cortex, functional connectivity, gene expression, macrocephaly, mouse

Introduction

Autism spectrum disorder (ASD) is diagnosed on the basis of socio-communicative deficits and repetitive, perseverative behaviors with restricted interests (APA 2013). ASD is frequently associated with comorbidities like hypersensitivity to sensory stimuli, seizures, and anxiety (Tavassoli et al. 2014; Croen et al. 2015; Jeste and Tuchman 2015). The phenotypic and genetic heterogeneity of ASD has hampered the elucidation of the molecular mechanisms that may underlie specific behavioral symptoms. However, the recent identification of de novo, likely gene disrupting (LGD) mutations that show highly significant associations with autism (Neale et al. 2012; Talkowski et al. 2012; O'Roak et al. 2012b; Iossifov et al. 2014; O'Roak et al. 2014) provides an opportunity to phenotype and molecularly characterize genetically defined ASD subtypes.

Exome sequencing studies of several thousand simplex families detected de novo, LGD mutations in the *CHD8* (Chromodomain Helicase DNA binding factor 8) gene (Neale et al. 2012; Talkowski et al. 2012; O'Roak et al. 2012b; Iossifov et al. 2014; O'Roak et al. 2014). Patients with *CHD8* mutations are characterized by a high incidence of autism, macrocephaly, facial dysmorphisms, motor delay and hypotonia, intellectual disability, and gastrointestinal problems (Bernier et al. 2014; Merner et al. 2016; Stolerman et al. 2016; Stessman et al. 2017). *CHD8* encodes an ATP-dependent chromatin remodeling protein of the chromodomain helicase DNA binding family (Yuan et al. 2007; Thompson et al. 2008). The recruitment of CHD8 to gene promoters in mouse and human neural progenitors is strongly associated with transcriptional activation, while *CHD8* knock-down in these cells results in the reduced expression of many ASD-associated genes (Sugathan et al. 2014; Cotney et al. 2015).

Three groups recently described *Chd8*$^{+/-}$ mouse models (Katayama et al. 2016; Gompers et al. 2017; Platt et al. 2017). Megalencephaly, subtle but wide-spread transcriptional changes and behavioral anomalies were found in all these *Chd8*$^{+/-}$ mouse lines. Individual studies reported attenuated expression of neural genes and derepression of REST (Katayama et al. 2016), alterations in striatal neurotransmission (Platt et al. 2017) and a developmental RNA splicing phenotype (Gompers et al. 2017). Understanding the contribution of each of these mechanisms to the ASD phenotype remains a major challenge.

Altered brain connectivity, characterized by local over-connectivity and long-range under-connectivity, has been hypothesized to underpin some of the neuropsychiatric phenotypes observed in ASD (Belmonte et al. 2004; Just et al. 2004). Resting-state functional MRI (rsfMRI) studies in ASD patients have provided evidence for reduced long-range synchronization in spontaneous brain activity (reviewed in Picci et al. 2016). Increased long-range connectivity has also been reported in a subset of cases (Di Martino et al. 2014), consistent with the phenotypic heterogeneity of ASD. Thus, the exact nature of aberrant functional connectivity in ASD may depend on the specific underlying aetiology.

Similar rsfMRI studies in ASD mouse models may help bridge the gap between ASD models and the human condition (Liska and Gozzi 2016). As one example, homozygous *Cntnap2* mouse mutants exhibit hypoconnectivity of the default mode network (Liska et al. 2017), a phenotype often observed in idiopathic ASD patients (Cherkassky et al. 2006) and recapitulating analogous clinical observations in humans with *CNTNAP2* mutations (Scott-Van Zeeland et al. 2010).

In the present study we generated a novel *Chd8*$^{+/-}$ mouse model. We report behavioral anomalies, macrocephaly and functional over-connectivity in cortico-hippocampal networks in these mice that are prefigured by dysregulation of the cortical transcriptome in the early postnatal period.

Methods

Chd8 Gene Targeting

A 14.84 kb genomic DNA fragment was subcloned from C57BL/6 BAC clone (RP23: 318M20) into pSP72 (Promega). This fragment encompassed a 9.45 kb 5′ long homology arm (LA) and a 4.4 kb 3′ short homology arm (SA). The targeting construct was generated by inserting a loxP/FRT-PGK-gb2-Neo cassette 214 bp 3′ of exon 3 (inGenious Targeting Laboratory [iTL], Ronkonkoma, NY, USA). An additional single loxP site containing a BclI restriction site for Southern blot screening was inserted 5′ of exon 3. The final targeting construct of 18.8 kb was linearized by NotI digestion and electroporated into C57BL/6 ES cells. G418-resistent clones were selected, screened by PCR and Southern blot for successful homologous recombination. Five clones with successful recombination were identified (Supplementary Fig. S1) and 2 clones (124 and 254) were injected into Balb/c blastocysts (iTL). Resulting chimaeras were bred with Flpe deleter mice on a C57BL/6J background to excise the neo cassette and produce *Chd8*$^{flox/+}$ mice (Supplementary Fig. S1). *Chd8*$^{flox/+}$ mice were then crossed with *β-actinCre* mice (Lewandoski and Martin 1997) to generate a *Chd8* null allele (*Chd8*$^{-}$). *β-actinCre;Chd8*$^{+/-}$ mice were crossed with C57BL/6J mice to remove the Cre transgene and establish a *Chd8*$^{+/-}$ line.

Mice

Experimental mice were produced by *Chd8*$^{+/-}$ × C57BL/6J crosses, taking care to equalize paternal or maternal inheritance of the *Chd8* null allele, especially for behavioral experiments. For genotyping, genomic DNA was extracted using Proteinase K digestion or the HotSHOT method (Truett et al. 2000). Genotyping reactions were then performed for the presence of *Chd8* wildtype and null alleles using the following primer pair: FW: CCC ACA TCA AGT GGC TGT AA, Rev: GGT AGG GAA GCA GTG TCC AG.

This reaction produces a PCR product of 395 bp for the null allele and 1.1 kb for the wildtype allele.

Western Blot

Telencephalic vesicles were dissected from E12.5 embryos and total cell protein prepared by lysing in 8 M urea, 1% CHAPS, 50 mM Tris (pH 7.9) containing protease inhibitors (PMSF, Pepstatin A, Leupeptin, Aprotinin; Roche) and a phosphatase inhibitor cocktail (Sigma). Samples were loaded (10 µg total protein per lane) onto a Mini-PROTEAN precast gel (Bio-Rad) and resolved using gel electrophoresis. Protein was transferred to a nitrocellulose membrane (Bio-Rad) which was then blocked in 5% nonfat milk powder (Bio-Rad) and 1% bovine serum albumin (BSA, Sigma) in TBS with 0.1% Tween-20 (TBST), followed by incubation with anti-CHD8 primary antibody (rabbit anti-Chd8 N-terminal, Bethyl Laboratories (cat#: A301-224 A), 1:5000) in 3% nonfat milk powder and 1% BSA in TBST overnight at 4 °C. After washing, the membrane was incubated with HRP-conjugated secondary antibody (Millipore), HRP detected with Clarity ECL reagent (Bio-Rad) and the membrane imaged using a Bio-Rad ChemiDoc system. The same membrane was subsequently incubated with anti-GAPDH primary antibody (rabbit anti-GAPDH, Abcam (cat#: ab9485), 1:40 000) overnight at 4 °C and probed with HRP-conjugate and imaged as before. Relative protein quantity was calculated using Bio-Rad ImageLab software.

X-ray Computed Tomography

Fixed heads from adult (26–27 days old) *Chd8*$^{+/-}$ and *Chd8*$^{+/+}$ mice (n = 7 of each from 2 different litters) were scanned using a GE Locus SP microCT scanner. The specimens were immobilized using cotton gauze and scanned to produce 28 µm voxel size volumes, using a X-ray tube voltage of 80kVp and a tube current of 80µA. An aluminum filter (0.05 mm) was used to adjust the energy distribution of the X-ray source. Reconstructions of computer tomography scans, images and measurements were done in MicroView 2.5.0 software (Parallax Innovations, ON, Canada). Each 3D landmark point was recorded, twice for each sample, using the 3D point recording built-in tool within the same software, with the operator blind to the genotypes. The distances between the landmarks were normalized for each sample to the average of the wild-type littermates. Graphics of the plotted data and statistical analysis were performed using GraphPad Prism version 6.0 h for Mac OS X (GraphPad Software, La Jolla, CA USA, www.graphpad.com). Unpaired Student *t*-tests were applied to analyze the variation between the 2 groups, for every distance between 2 specific 3D landmark points. 3D coordinate locations of a total of 22 biological relevant cranial landmarks were chosen based on a landmark list for adult mouse skull (Hill et al. 2009).

Behavioral Assessments

Mice for behavioral testing were housed, marked for identification and behaviors assessed essentially as described in Whittaker et al. (2017a). Different batches of mice were used for (1) recording pup USVs and spontaneous motor behaviors, and (2) adult behaviors (9–12 weeks of age at the start of testing; 19–22 weeks of age at the end of testing). For adult behaviors, tests were carried out in the following order: rotarod, grip strength, open field, self-grooming, marble burying, adult social investigation, 3 chamber social approach, light/dark test, olfactory habituation/dishabituation and Morris water maze.

General Activity Measurements

General activity was measured using a running wheel paradigm. Mice were housed individually under a 12 h:12 h light-dark cycle (lights on at 8 am; lights off at 8 pm) in a light-, air-, temperature-controlled ventilated cabinet (Arrowmight, Hereford, UK). Running-wheel cages were equipped with an infrared sensor (Bilaney consultant Ltd, Sevenoaks, UK) connected to a computer. Data were collected in 1-min bins using Clocklab software (Actimetrics, Inc, Wilmette, IL, USA). Mice were continuously monitored undisturbed from the day they were placed in the running wheel cages and their general activity during the light versus dark phase were compared over the first 7 days.

Structural MRI

After completion of adult behavioral tests, mice were terminally anesthetized and intracardially perfused. Samples were processed, imaged and analyzed as previously described (Whittaker et al. 2017b).

Resting-State fMRI

rsfMRI experiments were performed on 15–18 weeks old mice (n = 23 *Chd8*$^{+/+}$; n = 19 *Chd8*$^{+/-}$). Animals were prepared for imaging as previously described (Ferrari et al. 2012; Sforazzini et al. 2016). Briefly, mice were anesthetized using isoflurane (5% induction), intubated and artificially ventilated (2% maintenance). Blood pressure was monitored continuously by cannulating the left femoral artery, also allowing for terminal arterial blood sampling. Administration of isoflurane was ceased after surgery and substituted with halothane (0.75%). Functional data acquisition commenced 45 min after isoflurane cessation. To rule out possible genotype-dependent differences in anesthesia sensitivity we continuously recorded 2 independent readouts previously shown to be linearly correlated with anesthesia depth: arterial blood pressure and amplitude of cortical BOLD signal fluctuations (Steffey et al. 2003; Liu et al. 2011; Zhan et al. 2014). Arterial blood pressure (P = 0.79; Supplementary Fig. S5A) and the amplitude of BOLD signal fluctuations of motor cortex (P = 0.56; Supplementary Fig. S5B) did not significantly differ between *Chd8*$^{+/-}$ mice and littermate controls, eliminating a confounding contribution of anesthesia. In vivo images were obtained using a 7.0 T MRI scanner (Bruker Biospin, Milan), as previously described (Liska et al. 2017). Signal transmission and reception were achieved using a 72 mm birdcage transmit coil and a 4-channel solenoid coil. For each session, high-resolution anatomical images were acquired using a fast spin echo sequence based on the following parameters: repetition time (TR)/echo time (TE) 5500/60 ms, matrix 192 × 192, field of view 2 × 2 cm^2, 24 coronal slices, and slice thickness 0.5 mm. Cocentred BOLD rsfMRI time series were acquired using an echo planar imaging (EPI) sequence with the following parameters: TR/TE 1200/15 ms, flip angle 30°, matrix 100 × 100, field of views 2 × 2 cm^2, 24 coronal slices, slice thickness 0.5 mm, 500 volumes, and 10 min total acquisition time. Raw MRI data, templates, and code employed to generate functional maps are available by contacting AG.

Functional Connectivity Analyses

To allow for T_1 equilibration effects, the first 20 volumes of rsfMRI data were removed. The time series were then despiked, corrected for motion and spatially normalized to an in-house mouse brain template (Sforazzini et al. 2014). Normalized data had a spatial resolution of 0.1042 × 0.1042 × 0.5 mm^3 (192 × 192 × 24 matrix). Mean ventricular signal (averaged rsfMRI time course within a reference ventricular mask) and head motion traces

were regressed out of each time series. No genotype-dependent differences were observed in ventricular volume, as measured by the dimensions of individual ventricular masks. All rsfMRI time series were then spatially smoothed (full width at half maximum of 0.6 mm) and band-pass filtered using a frequency window of 0.01–0.1 Hz.

To identify brain regions displaying genotype-dependent differences in functional connectivity in an unbiased manner, we calculated global rsfMRI connectivity maps for all subjects, as described previously in detail (Liska et al. 2015, 2017). A previously described seed-based approach was then used to examine between-group differences in the intensity and scope of long-range rsfMRI correlation networks (Sforazzini et al. 2016).

Tissue Collection and Processing

Pups were weighed and sacrificed, while embryos were collected by dissection in ice-cold PBS, excess PBS drained and whole embryos weighed. Brains were then dissected from the skull in ice-cold PBS and cut below the brain stem, immediately drained on paper towels using a slotted spoon and wet weights determined using a fine scale. Brain weights were normalized to body weight and group differences were calculated using unpaired student's *t*-test. Brains were postfixed in 4% PFA at 4 °C for 24 h, dehydrated and paraffin embedded. Serial coronal sections were cut at 10 µm such that each slide contained 3 consecutive sections.

Immunohistochemistry

Sections were rehydrated using standard protocols and heated in 10 mM Sodium Citrate solution (pH 6). Endogenous peroxidases were blocked by incubating in 3% H_2O_2 and 10% MeOH in PBS for 15 min. Sections were permeabilised in 0.2% Triton X-100 (Sigma-Aldrich) in PBS (PBT2) for 5 min and blocked using 10% heat-inactivated normal goat serum and 2% gelatin in PBT2 for 1 h. Sections were incubated in 5% GS in PBT2 containing primary antibody (rabbit anti-phosphohistone 3B (Cell Signaling (#9701), 1/100) overnight at 4 °C. After incubation with primary antibody, sections were incubated in biotinylated anti-rabbit immunoglobulin secondary antibody (Dako (#E0432), 1/200) in 5% goat serum in PBT2. Samples were washed in PBS and incubated with avidin/biotin complex (ABC, Vector) in PBS for 1 h. Sections were developed using 0.025% DAB and 0.03% H_2O_2 in PBS for 10 min, counterstaining using Ehrlich's Hematoxylin solution and mounted in DPX (Sigma-Aldrich). Images were acquired on a Nikon 80i microscope equipped with a Nikon 5 M pixel Nikon DS digital camera. Images were processed using Adobe Photoshop and Illustrator.

RNA Extraction and qRT-PCR Analysis

To extract RNA, dissected cortices were lysed in 600 µl Trizol (Life Technologies). RNA was purified and DNase-treated using the Direct-zol RNA MiniPrep kit (Zymo Research) according to the manufacturer's instructions. For qRT-PCR, cDNA was synthesized using 200 ng RNA from 4 biological replicates per condition with the Precision nanoScript 2 Reverse Transcription Kit (PrimerDesign Ltd.) according to the manufacturer's recommendations. qRT-PCRs were performed on a Stratagene Mx3000p (Agilent Technologies) using PrecisionPlus-MX 2× qPCR Mastermix with SYBR green (PrimerDesign Ltd.) and primers against *Chd8* exon 3–4 (FW: CAG AGG AGG AGG GTG AAA AGA AAC, Rev: GAG TTG TCA GAC GAT GTG TTA CGC) or *Chd8* exon 1–2 (FW: TGA AGC CTG CAG TTA CAC TGA CGT, Rev: CTG CGG CTG TGG CTG TGG TT). *Canx* and *Sdha* (E12.5) and *Gapdh* and *Eifa* (P5) were used as endogenous control genes as determined by prior geNorm (Primerdesign, UK) analysis for the respective sample sets. Relative expression levels were calculated using the $2^{-\Delta\Delta CT}$ method.

RNA Sequencing

RNA was isolated from microdissected cortices at E12.5 (both hemispheres) and P5 (one hemisphere) and reverse transcribed (n = 3 per experimental group). cDNA was end-repaired, adaptor-ligated, and A-tailed. Paired-end sequencing was performed on the Illumina HiSeq 4000 platform. Quality of the raw sequencing data was checked using FastQC version 0.11.2 (Andrews 2010; available at: http://www.bioinformatics.babraham.ac.uk/projects/fastqc) and trimming of adaptor sequences was performed using Trim Galore! version 0.4.1 (Krueger 2012; available at: http://www.bioinformatics.babraham.ac.uk/projects/trim_galore/). Reads were aligned to the mouse genome (GRCm38.p4) using Tophat version 2.1.0 and aligned reads were counted using FeatureCounts version 1.5.0 (Kim et al. 2013; Liao et al. 2014). Differential expression testing was performed using DESeq2 version 1.10.1, as previously described (Love et al. 2014). Gene ontology analysis and functional classification was performed using DAVID with all detected DEGs below a 0.05 FDR (Huang et al. 2009). Putative regulatory transcription factors were determined with Enrichr using the "ENCODE and ChEA Consensus TFs from ChIP-X" database with all DEGs below a 0.05 FDR (Chen et al. 2013). The R package ggplot2 version 2.1.0 was used to generate volcano plots. The list of ASD-associated genes used for overlap with P5 DEGs was obtained from the SFARI Gene Scoring module (https://gene.sfari.org/autdb/HG_Home.do). RNA-seq data have been deposited into GEO, accession number GSE81103.

Gene Expression Enrichment Analysis

In total, 4345 gene expression images corresponding to 4082 unique genes were downloaded from the Allen Institute's Mouse Brain Atlas coronal expression dataset (Lein et al. 2007). The coronal expression dataset is limited by the fact that it only partially covers the genome and was defined in a biased manner (Ng et al. 2009). However, it offers higher data quality and resolution especially in lateral cortical areas including auditory cortex, compared with the sagittal dataset. This dataset, obtained via in situ hybridization, consisted of 3D spatial expression images aligned to a single reference model and summarized over the whole mouse brain at a 200 µm isotropic resolution. Specifically, the gene expression energies, defined by the Allen Institute as the sum of expressing pixel intensities divided by the sum of all pixels in a subdivision, were obtained. Expression data were obtained from adult (P56) male C57Bl/6.

Mean gene expression energies were extracted under a set of Allen Institute-defined segmentations, resulting in vectors of expression values for each gene that describe their spatial expression patterns. To account for differences in probe affinities that subsequently affect the total expression levels reported in the images, expression values for each gene were further normalized by dividing by the total expression (summed over regions) for that gene.

Next, we extracted rsfMRI time series data under the aforementioned set of segmentations. This was achieved by aligning, via ANTS (Avants et al. 2009; available at: http://hdl.handle.net/10380/3113), the Allen Institute's average 2-photon microscopy

template over which the parcellations were defined to a high-resolution (56 μm) T2-weighted MR template of the mouse brain, resulting in an atlas defined on MRI data. This atlas was then combined with the MAGeT procedure (Chakravarty et al. 2013) implemented in the PydPiper framework (Friedel et al. 2014) to generate segmentations for each of the T2-weighted images acquired during the course of the rsfMRI experiments.

We focused on the pair of regions that showed strongest over-connectivity under these parcellations and determined candidate genes by choosing those that had the highest normalized expression in both regions, compared with all other genes. Candidates that were in the top 20% of genes for both regions were passed through an enrichment analysis via the GOrilla tool (Eden et al. 2009; http://cbl-gorilla.cs.technion.ac.il/). Another set of candidates were obtained by ranking each gene by the sum of their normalized expression values in both regions (equivalent to the L1 distance); this set also favors genes with high expression in one of the 2 regions, along with both regions. For enrichment analyses of ranked lists of genes, GOrilla automatically thresholds the list independently for each GO term so that the optimal enrichment is found (Eden et al. 2009).

To establish specificity of the enriched gene ontology terms, we performed equivalent analyses between 10 randomly chosen regional pairs (DG–FRP, LA–MB, OLF–IG, BLA–P-sat, MY-sat–DG, PAL–GU, P-sat–LZ, PAA–VERM, AON–HEM, MY-mot–MB). The number of returned GO terms was generally low and did not show an enrichment for neuronal development terms.

Statistical Analysis

Data are reported as mean ± standard error of the Mean (SEM) and graphs show all individual data points where feasible. Significant *P*-values are reported in the results section and figure legends provide full details of all relevant statistical parameters including group sizes. Statistical analyses were performed either with SPSS (Version 22, IBM, Armonk, USA) or GraphPad Prism (Version 6, GraphPad Software, La Jolla, CA, USA). All analyses were performed blind to genotype.

Behavior

Data were analyzed using either a between-subjects ANOVA or a 2-way repeated measures ANOVA, as appropriate. If there was no statistically significant sex difference, data were pooled. When the appropriate ANOVA showed a significant effect for a particular task, student's *t*-tests were used as post hoc analyses, as there were only 2 groups for comparison. Cohort details can be found in the methods, group sizes are stated in the figure legend.

Proliferation

Phosphohistone 3B-positive cells lining the ventricular surface of the dorsal cortex were counted and normalized to the length of ventricular surface. These were quantified on both sides of the brain in 3 consecutive sections and averaged to calculate the number of phosphohistone 3B-positive cells per μm of ventricular surface in the dorsal cortex. Group differences were calculated using unpaired student's *t*-test.

μCT Analysis

Each 3D landmark point was recorded twice for each sample and distances between landmark points normalized to the average of the wildtype controls. Group differences for distances between 2 specific 3D landmark points were calculated using unpaired student *t*-test.

MRI Analyses

Processing of raw data is described in detail in the relevant method sections. For structural MRI, significant differences were determined between groups for the 159 different regions in the brain. Voxelwise comparisons were made between mutants and littermate controls, group differences were calculated using unpaired student's *t*-test and multiple comparisons were controlled for using a false discovery rate (FDR < 0.15). Exact *P*-values can be found in Supplementary Table S1.

For rsfMRI studies, group-level differences in connectivity distributions were calculated using 2-tailed student's *t*-test ($P < 0.05$, family-wise error cluster-corrected, with cluster-defining threshold of $t_{24} > 2.06$, $P < 0.05$) and multiple comparisons were controlled for using an FDR < 0.05.

RNA-seq

Processing of raw data and differential expression testing is described in Methods. Multiple comparisons were controlled for using an FDR < 0.05. Exact *P*-values and FDR adjusted *P*-values for all differentially expressed genes (DEGs) are listed in Supplementary Tables S2 and S3.

Results

A mouse line with a conditional *Chd8* allele was produced through homologous recombination in C57Bl/6 embryonic stem cells (Supplementary Fig. S1A, B). $Chd8^{flox}$ mice were crossed with the ubiquitously expressing *β-actin*Cre line (Lewandoski and Martin 1997) to generate $Chd8^{+/-}$ mice (Supplementary Fig. S1C). Cre-mediated deletion of *loxP*-flanked (flox) exon 3 results in an early frameshift and termination of translation at amino acid 419, predicted to produce a protein that lacks all functional domains, equivalent to nonsense and frameshift mutations terminating CHD8 at amino acids 62 and 747 in patients (Barnard et al. 2015).

Quantitative RT-PCR (qRT-PCR) on RNA isolated from E12.5 and P5 neocortices using primers spanning the exon 3/4 boundary showed *Chd8* expression reduced by 64% ($P = 0.006$) and 52% ($P = 0.01$), respectively (Supplementary Fig. S1D). CHD8 protein levels were reduced by 51% in $Chd8^{+/-}$ E12.5 neocortices compared with controls (Supplementary Fig. S1E, F), validating our $Chd8^{+/-}$ mice as a suitable model for *CHD8* haploinsufficiency. Importantly, we found no evidence for a truncated protein product of 419aa (~45 kDa) that may have resulted from translation of any mutant transcript (Supplementary Fig. S1E). qRT-PCR analysis at E12.5 with primers spanning the exon 1/2 boundary (upstream of the recombination event) revealed reduced *Chd8* expression of 52% (Supplementary Fig. S1G), indicating that the mutant transcript is most likely subject to nonsense-mediated decay.

Chd8 Heterozygous Mice Have Specific Craniofacial and Structural Brain Phenotypes

Humans with truncating mutations in a single *CHD8* allele often present with macrocephaly (64%) and distinct craniofacial phenotypes (89%), which include hypertelorism (wide-set eyes, 67%) (Bernier et al. 2014; Stessman et al. 2017). We characterized the cranioskeleton of $Chd8^{+/-}$ mice by μCT to ask whether these phenotypes were also present in $Chd8^{+/-}$ mice (Fig. 1A–D). The interorbital distance (landmarks 8–9, Fig. 1C,D) was

significantly wider in *Chd8*$^{+/-}$ mice compared with controls, indicative of a hyperteloric phenotype (*P = 0.0273; Fig. 1C,D,F). In addition, the anterior–posterior length of the interparietal bone (landmarks 4–5) is increased in *Chd8*$^{+/-}$ animals (**P = 0.0025; Fig. 1A,B,E), suggestive of more wide-spread craniofacial anomalies associated with *Chd8* haploinsufficiency.

To examine whether structural brain abnormalities were present in *Chd8*$^{+/-}$ mice, their brains were compared with *Chd8*$^{+/+}$ littermates by high-resolution MRI (Fig 1G). Total brain volume was increased by 2.7% in *Chd8*$^{+/-}$ mice (476 vs. 463 mm^3, P = 0.048, FDR = 15%, Fig. 1H). Accordingly, several brain regions, including cortical areas, hippocampus and parts of the cerebellum showed volumetric increases (Fig. 1G,H, Supplementary Table S1). Structural alterations of these brain areas have been implicated in autism (Blatt 2012; Ecker 2016; Donovan and Basson 2017) providing potential neural substrates for the autism phenotype associated with *CHD8* haploinsufficiency in humans.

Chd8$^{+/-}$ Mice Show Abnormal Activity Levels and Differences in Social Interaction

We next assessed *Chd8*$^{+/-}$ mice in a number of behavioral tests to ask whether they exhibited any signs of socio-communicative deficits, repetitive behaviors or cognitive inflexibility, representing core ASD-like behaviors in humans.

Chd8 heterozygous pups displayed signs of delayed motor development in the first 2 weeks after birth. *Chd8*$^{+/-}$ pups took slightly longer than wildtype littermates to develop an effective righting reflex over time (*P = 0.014; Fig. 2A). Correspondingly, *Chd8*$^{+/-}$ pups spent more time engaged in unsuccessful attempts to turn over on their stomachs as measured during the spontaneous motor behavior observations (P6: *P = 0.0312, P8: *P = 0.0354; Fig. 2B). Once they were able to move around the cage, mutant pups spent on average more time in locomotion than wildtype littermates suggestive of hyperactivity (**P = 0.009; Fig. 2C).

In the 3-chamber sociability test, adult *Chd8*$^{+/-}$ mice spent significantly more time in the chamber with the novel age- and sex-matched conspecific mouse than in the other chambers, indicative of normal sociability (Fig. 2D). Interestingly, rather than displaying sociability deficits, mutant mice spent slightly, but significantly more time in the chamber containing the mouse, compared with controls (*P = 0.029; Fig. 2D). *Chd8*$^{+/-}$ mice also spent more time investigating conspecific mice in a reciprocal social interaction test (*P = 0.015; Fig. 2E). A quantitative olfactory habituation/dishabituation test revealed an increased interest in an odour with social significance (urine) in *Chd8*$^{+/-}$ mice compared with controls (*P = 0.03, ***P = 0.0002; Fig. 2F). No difference in the time spent investigating a nonsocial (banana) odour was observed, implying an increased interest specifically in social cues and an otherwise normal capacity for odour discrimination (Fig. 2F).

Examination of these animals in the open field arena revealed a marked hypoactivity in *Chd8*$^{+/-}$ mice (***$P = 10^{-9}$; Fig. 2G,H). The hypoactive phenotype was also observed in mutant mice in their homecage environment by measuring activity on a running wheel over a 1-week period (*P = 0.019; Fig. 2I). The open field test did not show any evidence of anxiety in these mice, that is, an increased reluctance to enter the inner, most exposed area of an open field arena (Fig. 2J). This was confirmed in the light/dark box test that showed no difference between wildtype and mutant mice (Fig. 2K). Forelimb grip strength was slightly but significantly reduced in mutant mice (*P = 0.045 [males] *P = 0.042 [females]; Fig 2L) but *Chd8*$^{+/-}$ mice showed normal motor abilities on the revolving rotarod, indicating that a reduced capacity to perform motor tasks was unlikely to be the cause of the hypoactive phenotype (Fig. 2M). No evidence of repetitive behaviors was observed by assessing marble burying and self-grooming behaviors (Fig. 2N, O). In fact, mutants showed slightly delayed marble burying behavior, most likely due to their general hypoactivity (*P = 0.04, ***P = 0.0004; Fig. 2N).

Spatial learning abilities and cognitive flexibility were assessed in the hippocampus-dependent Morris water maze test. *Chd8*$^{+/-}$ mice performed normally in the learning part of this test (Fig. 2P). In a reversal paradigm, these mice were also indistinguishable from wildtype littermates, implying normal cognitive, spatial learning abilities and flexibility (Fig. 2P). Finally, no differences in the number of ultrasonic vocalizations (USVs) of pups separated from the nest were recorded, indicating no obvious communication deficits (Fig. 2Q).

As male mice from this adult behavioral cohort were used for structural MRI analyses (Fig. 1G,H) we were able to correlate their brain volume with specific behaviors. We observed significant inverse correlations between activity in the open field and hippocampal volume (*P = 0.012; Supplementary Fig. S3A), as well as cortical volume (*P = 0.036; Supplementary Fig. S3B). Overall brain volume and hypoactivity showed a weaker correlation (P = 0.092; Supplementary Fig. S3C) hinting at a degree of specificity for cortical and hippocampal regions.

In summary, *Chd8*$^{+/-}$ mice displayed no socio-communicative deficits, but rather exhibited a heightened interest in social cues. No evidence for perseverative and repetitive behaviors were observed. *Chd8*$^{+/-}$ pups showed evidence for hyperactivity and delayed motor development while adult *Chd8*$^{+/-}$ mice exhibited a hypoactive phenotype, which was significantly correlated with overgrowth in cortical and hippocampal regions.

Chd8 Haploinsufficiency Causes General Growth Delay but Postnatal Brain Overgrowth

To determine whether the brain overgrowth phenotype was already present at early postnatal stages when developmental delay was evident, we measured body and brain weights from birth. *Chd8*$^{+/-}$ pups showed significant growth retardation from postnatal day 4 onwards and into early adulthood (Fig. 3A). Brain and body weight were well correlated in both wildtype and heterozygous mice at P35 (r^2 = 0.25, P = 0.0004 and r^2 = 0.28, P = 0.005, respectively), with *Chd8* mutants displaying higher brain weights compared with their wildtype littermate controls with equivalent body weight (Fig. 3B). A group-wise comparison confirmed the significant increase in normalized brain weight in *Chd8*$^{+/-}$ mice compared with wildtype littermates (20.4% increase, ***P < 0.0001; Fig. 3C). At P7, normalized brain weights were already significantly larger in *Chd8*$^{+/-}$ pups compared with wildtype littermate controls (9.3%, ***P = 0.0009) with more subtle differences between the groups observed at P0 (6.7%, *P = 0.01).

Together, these analyses suggested that subtle, but cumulative differences in brain growth over time may be responsible for small increases in brain size. Indeed, we did not detect any significant differences in cortical ventricular zone (VZ) proliferation as measured by phosphohistone H3 immunostaining at E12.5, E16.5, or P0 (Fig. 3E,F). However, subtle increases in progenitor proliferation in the VZ cannot be completely ruled out.

CHD8 Controls the Expression of ASD-Associated Axon Guidance Genes in the Early Postnatal Neocortex

To gain insights into the transcriptional programs that may underlie the subtle brain overgrowth and abnormal behaviors

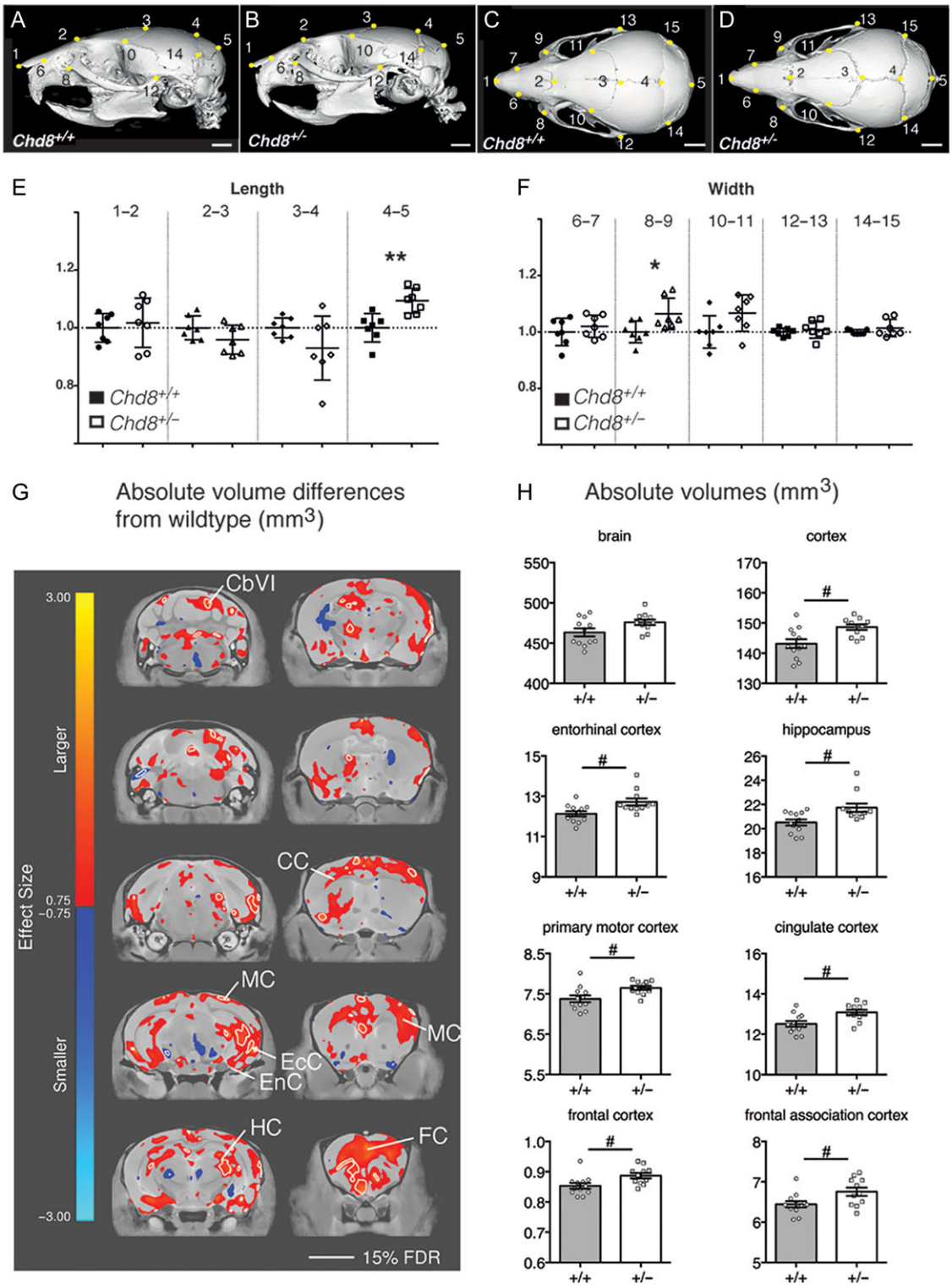

Figure 1. Hypertelorism and mild megalencephaly in *Chd8*$^{+/-}$ mice. (*A–D*) Representative lateral (*A*,*B*) and dorsal (*C*,*D*) μCT views of 3D reconstructed skulls from mice with the indicated genotypes. Landmarks from 1 to 15 are indicated by yellow dots. Scale bars = 2 mm. (*E*,*F*) Graphs for measurements between indicated landmarks, normalized to average measurements from corresponding wildtype littermates. Mean ± SEM; landmarks 4–5: $P = 0.0025$, $t = 3.797$; landmarks 8–9: $P = 0.0273$, $t = 2.512$; df = 12, student's *t*-test, $n = 7$ per genotype. (*G*) High-resolution 7 T structural MRI coronal images of *Chd8*$^{+/-}$ brains from posterior (top left) to anterior (bottom right) are shown. Absolute volumetric differences in size, relative to wildtype controls are colored according to the scale on the left. Effect size is measured in units of standard deviation. Some regions with enlarged volumes are labeled as follows: CbVI = cerebellar lobule VI, MC= motor cortex, EcC = ectorhinal cortex, EnC = entorhinal cortex, HC = hippocampus, CC = cingulate cortex, FC =frontal association cortex. (*H*) Absolute volumes (mm^3) are plotted for whole brain, neocortex, and several other brain regions for the different genotypes as indicated. #FDR < 0.15, student's *t*-tests: brain: $P = 0.0484$, $t = 2.096$; cortex: $P = 0.0055$, $t = 3.093$; entorhinal cortex: $P = 0.011$, $t = 2.788$; hippocampus: $P = 0.0091$, $t = 2.873$ primary motor cortex: $P = 0.0126$, $t = 2.727$; cingulate cortex: $P = 0.0074$, $t = 2.965$; frontal cortex: $P = 0.0154$, $t = 2.639$; frontal association cortex: $P = 0.0238$, $t = 2.438$; df = 21, *Chd8*$^{+/-}$: $n = 11$, *Chd8*$^{+/+}$: $n = 12$. Individual volumes and volume differences for all brain regions are listed in Supplementary Table S1.

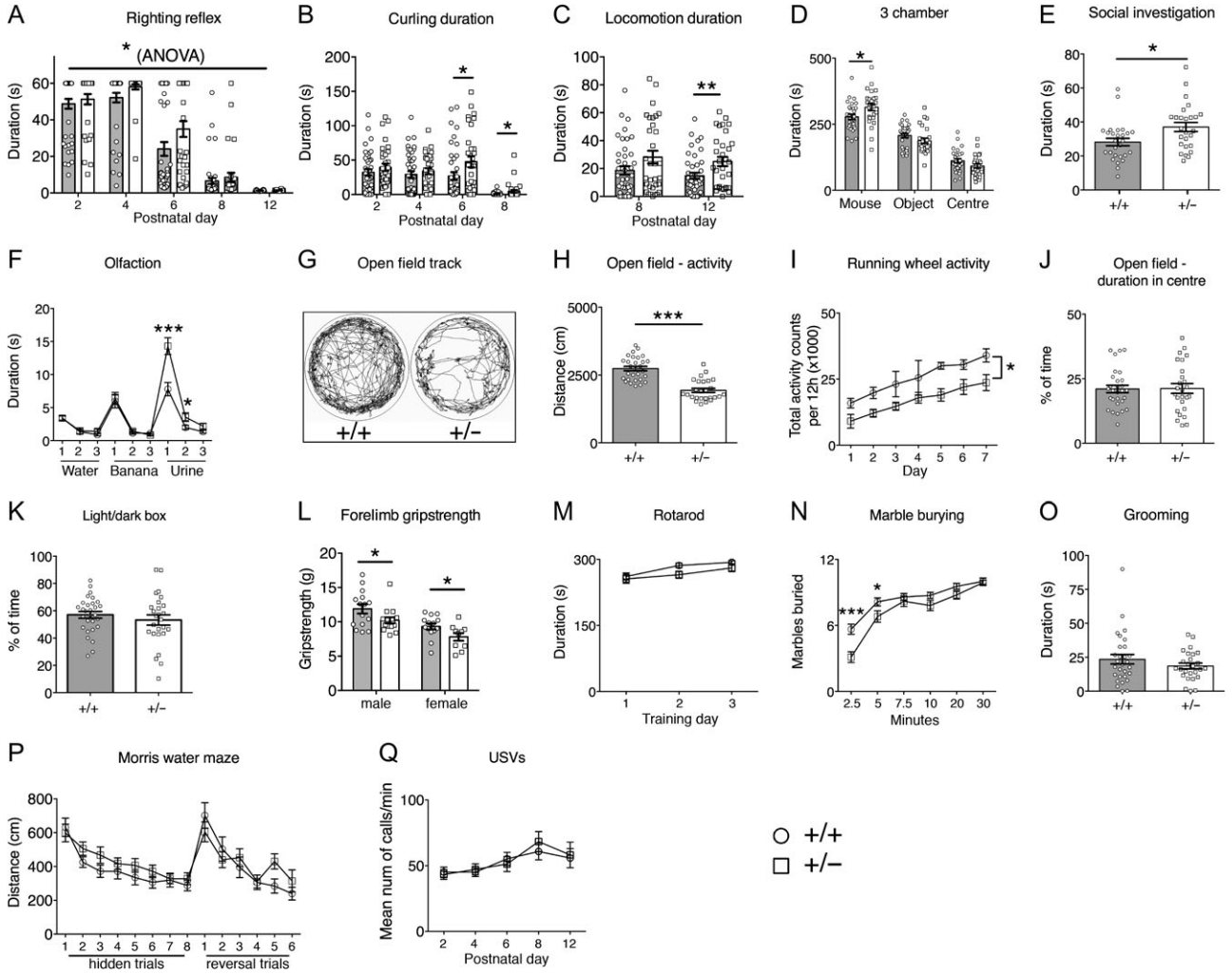

Figure 2. Complex behavioral abnormalities in *Chd8* heterozygous mice. (*A–Q*) Behavioral assessments of a cohort of adult *Chd8*$^{+/-}$ (+/−, $n = 16$ [male], $n = 14$ [female]) and *Chd8*$^{+/+}$ (+/+, $n = 15$ [male], $n = 14$ [female]) and of pup *Chd8*$^{+/-}$ (+/−, $n = 11$ [male], $n = 20$ [female]) and *Chd8*$^{+/+}$ (+/+, $n = 22$ [male], $n = 20$ [female]) animals. (*A*) The development of the righting reflex in pups at the indicated postnatal days. Pups failing to right by the end of the 60 s test period were given a score of 60 s. Note the significant delay in the acquisition of the full righting reflex response in *Chd8*$^{+/-}$ animals compared with littermate controls. Mean ± 1SEM; *P = 0.014 (one-way repeated-measures ANOVA: $f[1,72] = 6.36$ (between-subjects effect)). (*B*) The duration, in seconds, pups spent rolling on their back (curling) as recorded during the analysis of spontaneous movements during USV recordings. Note that *Chd8*$^{+/-}$ mice spent significantly more time curling at P6 and P8 compared with littermate controls. Mean ± SEM; P6 *P = 0.0312, P8 *P = 0.0354 (one-way repeated-measures ANOVA: $f[1,72] = 12.64$, $P = 0.001$ [between-subjects effect], with student's *t*-test as post hoc analysis) (p6: df = 72, $t = 2.197$, P8: df = 72, $t = 2.145$). (*C*) The duration, in seconds, pups spent in locomotion as recorded during the analysis of spontaneous movements during USV recordings. At P12 *Chd8*$^{+/-}$ animals spent significantly more time in locomotion as compared with littermate controls. Mean ± 1SEM, **P = 0.009 (one-way repeated measures ANOVA: ($f[1,72] = 7.33$, $P = 0.008$ [between-subjects effect], with student's *t*-test as post hoc analysis df = 72, $t = 2.687$). (*D*) The duration, in seconds, spent in each chamber of the 3-chamber sociability test. All mice spent a significantly higher proportion of time in the chamber with the age- and sex-matched stranger conspecific mouse compared with the other chambers. Mean ± SEM; *P = 0.029 (between-subjects ANOVA: $f[1,53] = 5.031$). (*E*) Duration, in seconds, of social investigation over a 3-min period. Social investigation was defined as the combined total duration of head, body and anogenital sniffing of a conspecific mouse. Mean ± SEM; *P = 0.015 (between-subjects ANOVA $f[1,52] = 6.307$). (*F*) Graph demonstrating the performance in the olfactory habituation/dishabituation test. Mean ± SEM; *P = 0.03, **P = 0.0002 (repeated-measures ANOVA: $f[2.85,145.23] = 9.24$, $P = 0.00002$, with student's *t*-test as post hoc analysis **df = 53, $t = 4.04$, *df = 53, $t = 2.23$). (*G*) Representative ethovision tracks of a *Chd8*$^{+/-}$ (+/−) and *Chd8*$^{+/+}$ (+/+) animal plotting their movements during the 10-min open field task. (*H*) The total distance traveled in the outer part of the open field arena over a 10-min time-period. Mean ± SEM; ***$P = 2 \times 10^{-9}$ (between-subjects ANOVA: $f[1,53] = 52.72$). (*I*) The total activity counts per 12 h period on running wheels in the homecage during 7 days of dark-phase recording. Mean ± SEM; *P = 0.019 (repeated-measures ANOVA: $f[1,7] = 9.12$, between-subjects effect). (*J*) The percentage of time spent in the center of the open field arena during the 10-min test. Mean ± SEM (between-subjects ANOVA: $f[1,53] = 0.007$, $P = 0.93$). (*K*) The percentage of time spent in the light chamber during the 5 min light/dark test. Mean ± SEM (between-subjects ANOVA: $f[1,51] = 0.824$, $P = 0.368$). (*L*) The average of 3 measurements of forelimb grip strength on a Linton Grip Strength meter. Mean ± SEM, males: *P = 0.045 (between-subjects ANOVA: $f[1,29] = 4.371$) females: *P = 0.042 (between-subjects ANOVA: $f[1,22] = 4.677$). (*M*) The mean latency of mice to fall from the rotarod. Mean ± SEM (repeated-measures ANOVA: $f[1.644,102] = 0.620$, $P = 0.540$). (*N*) The average number of marbles buried, out of a maximum of 12, within a 30-min time period. Mean ± SEM; *P = 0.04, ***P = 0.0004, (repeated-measures ANOVA: $f[3.66,265] = 4.70$, $P = 0.002$, with student's *t*-test as post hoc analysis *df = 53, $t = 2.12$, ***df = 53, $t = 3.79$). O) The duration, in seconds, mice spent self-grooming during the 10-min self-grooming test. Mean ± SEM (between-subjects ANOVA: $f[1,51] = 1.21$, $P = 0.28$). (*P*) Graph plotting the average distance swum for 4 trials daily over 8 consecutive training days to find the hidden platform (hidden trials), followed by 6 training days where the location of the platform was reversed (reversal trials). Mean ± SEM (repeated-measures ANOVA: $f[8.761,714] = 1.064$, $P = 0.388$). (*Q*) The mean number of ultrasonic vocalizations per minute on indicated postnatal days. Mean ± SEM (repeated-measures ANOVA: $f[1,72] = 0.76$, $P = 0.39$).

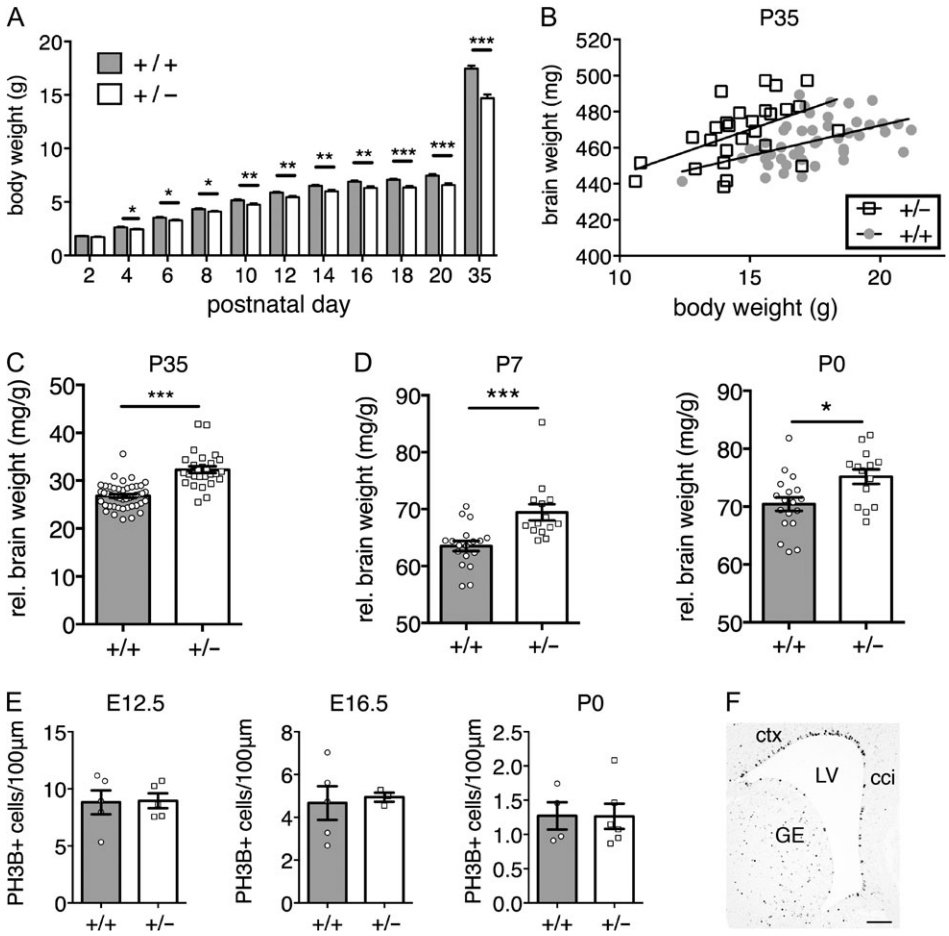

Figure 3. *Chd8* mutants display postnatal brain overgrowth. (*A*) Body weights of mice between P2 and P35. Repeated-measures ANOVA with student's *t*-test as post hoc analysis. ANOVA: $f(2.303, 158.940) = 12.313$, $P = 0.000003$; student's *t*-tests: P4: $t = 2.498$, $^{*}P = 0.0148$; P6: $t = 2.385$, $^{*}P = 0.0197$; P8: $t = 1.916$, $^{*}P = 0.0593$; P10: $t = 2.808$, $^{**}P = 0.0064$; P12: $t = 2.803$, $^{**}P = 0.0065$; P14: $t = 2.018$, $^{**}P = 0.0035$; P16: $t = 3.353$, $^{**}P = 0.0013$; P18: $t = 4.082$, $^{***}P = 0.0001$; P20: $t = 4.269$, $^{***}P < 0.0001$; P35: $t = 6.334$, $^{***}P < 0.0001$; df = 71, +/+, $n = 46$; +/−, $n = 27$. (*B*) Individual wet brain weights plotted against individual body weights for *Chd8*$^{+/-}$ (+/−), mice and their littermate controls (+/+) at postnatal day (P)35. Note that *Chd8*$^{+/-}$ mice have larger brain weights than littermate controls of equivalent body weight. Linear regression analysis: $r^2 = 0.25$, $P = 0.0004$ (+/+), $r^2 = 0.28$, $P = 0.005$ (+/−). (*C*) Wet brain weights normalized to body weight P35. *Chd8*$^{+/-}$ (+/−) show significantly increased normalized brain weights compared with their littermate controls (+/+). Mean ± SEM; $^{***}P < 0.0001$, $t = 7.455$ (student's *t*-test). +/+, $n = 46$; +/−, $n = 27$. D) Wet brain weights of pups at P7 and P0 normalized to body weight. *Chd8*$^{+/-}$ (+/−) pups show significantly larger normalized brain weights than their littermate controls (+/+) at P7 and P0. Mean ± SEM; $^{*}P = 0.01$, $t = 2.746$; $^{***}P = 0.0009$, $t = 3.681$ (student's *t*-test). P7: +/+, $n = 18$; +/−, $n = 14$; +/+; P0: +/+, $n = 18$; +/−, $n = 14$; +/+. (*E*) Quantification of phosphohistone H3 (PH3B) positive cells in the ventricular zone at E12.5, E16.5 and P0. Cell counts were normalized to ventricular surface length. Mean ± SEM; student's *t*-test. E12.5: +/+, $n = 5$; +/−, $n = 5$. E16.5: +/+, $n = 5$; +/−, $n = 3$. P0: +/+, $n = 4$; +/−, $n = 6$. (*F*) Example of PH3B immunostaining in an E16.5 coronal brain section. Scale bar = 100µm; LV: lateral ventricle, ctx: cortex, cci: cingulate cortex, GE: ganglionic eminence.

observed in *Chd8*$^{+/-}$ mice, we performed RNA-seq analysis on dissected neocortical tissue at 2 stages: (1) At E12.5, when *Chd8* expression peaks (Durak et al. 2016) and neural progenitor cells predominate; and (2) At P5, when many developmental processes with relevance for ASD aetiology, such as axon growth and guidance and synaptogenesis, are under way.

Surprisingly, only 5 genes, including *Chd8*, showed significant (FDR < 0.05) differential expression in *Chd8*$^{+/-}$ embryos at E12.5 in this experiment (Fig. 4A, Supplementary Table S2). By contrast, 649 DEGs (FDR < 0.05) were identified in the P5 neocortex, with over two-thirds of these genes downregulated (Fig. 4B, Supplementary Table S3).

Comparing all DEGs from the P5 dataset with the SFARI autism gene list identified 56 shared genes, representing a highly significant enrichment of ASD-associated genes in the DEG set ($P = 1.06 \times 10^{-10}$ [OR = 2.87]; Fig. 4C, Supplementary Table S4). Almost all (53/56 = 95%) of these ASD-associated genes were downregulated (Supplementary Table S4). We also overlapped our gene set with high confidence (SFARI categories 1 and 2) ASD candidates ($P = 3.26 \times 10^{-4}$ [OR = 4.61]; Fig. 4D). Nine genes, representing 16% of all SFARI categories 1 and 2 genes, were present in our DEG set at P5. All of these high confidence ASD candidate genes were downregulated (Supplementary Table S4).

Amongst the upregulated gene set, the most significant KEGG pathways, molecular functions and biological processes were related to protein transport, the ribosome and oxidative phosphorylation, whereas the downregulated gene set included categories related to cell adhesion, axonal guidance and calcium signaling pathways (Fig. 4E, F, Supplementary Fig. S2A, Supplementary Tables S5–10). Identification of potential regulatory transcription factors was performed using Enrichr, which found over-representation of Suz12 targets in the downregulated gene set (Supplementary Fig. S2B). Suz12 is a component

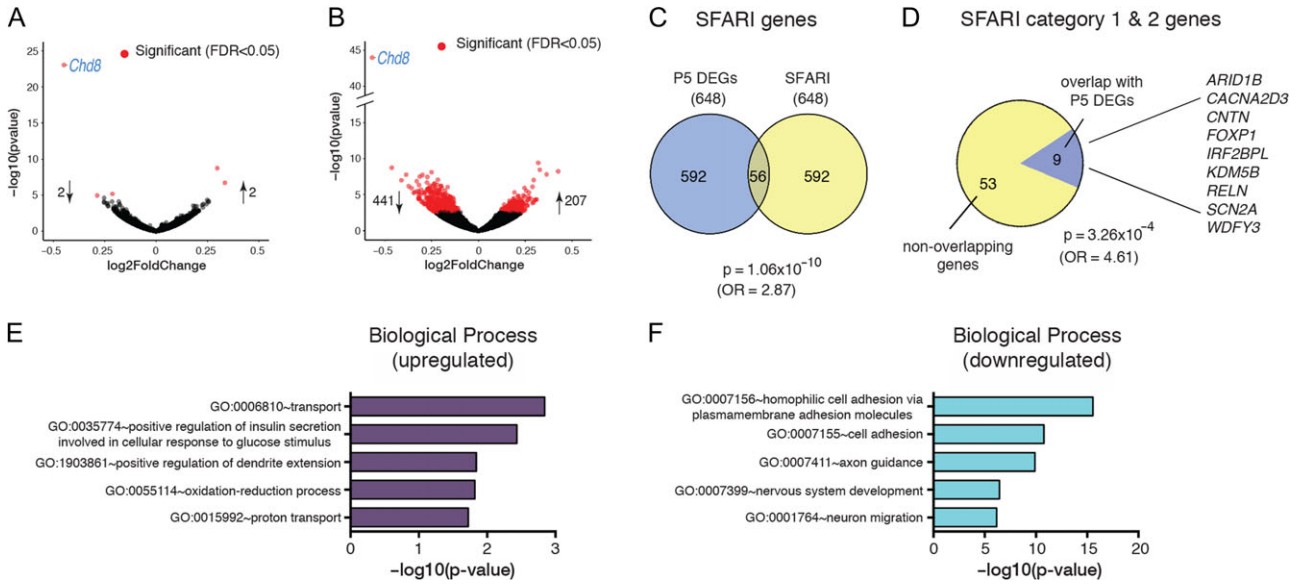

Figure 4. Gene expression changes in *Chd8*-deficient neocortices. (*A*) Volcano plot of RNA-seq data from embryonic (E12.5) *Chd8*$^{+/-}$ neocortex. Each point represents an individual gene and all genes differentially expressed in *Chd8*$^{+/-}$ samples with an FDR of 0.05 are highlighted in red. All differentially regulated genes are listed in Supplementary Table S2. (*B*) Volcano plot indicating differentially expressed genes (DEGs) detected by RNA-seq in P5 *Chd8*$^{+/-}$ neocortex. All differentially regulated genes are listed in Supplementary Table S3. (*C*) Venn diagram showing extent of overlap between P5 DEGs and ASD-associated genes (categories 1–5 and S) in the SFARI gene database. Enrichment was calculated using Fisher's exact test for count data. SFARI genes that overlap with P5 DEGs are listed by category in Supplementary Table S4. (*D*) Pie chart showing the proportion of high confidence ASD candidate genes (categories 1–2) that are found in the P5 DEG set. Enrichment was calculated using Fisher's exact test for count data. (*E*, *F*) Results of gene set enrichment analysis using the DAVID knowledgebase on the P5 DEG set (FDR < 0.05). The 5 most significant Gene Ontology terms in the Biological Processes category are shown for upregulated DEGs (*E*) and downregulated DEGs (*F*), respectively. The 5 most significant Gene Ontology terms in the molecular function and pathways categories and the 4 most over-represented transcription factors identified by Enrichr analysis are shown in Supplementary Figure S2. A comprehensive list of all significant Gene Ontology terms in the biological processes, molecular functions and pathways categories is given in Supplementary Tables S5–10.

of the Polycomb repressor complex 2 (PCR2) and is required for both histone methyl transferase and gene silencing activities of PRC2 (Cao and Zhang 2004). The observation that Suz12 targets are over-represented in the downregulated gene set offers a potential mechanistic explanation for the downregulation of some of these genes. None of the genes that encode PRC2 subunits like Suz12 were differentially expressed at P5, excluding the possibility that increased PRC2 gene expression at this stage of development was responsible for repression of *Suz12* target genes in *Chd8* mutants.

Chd8$^{+/-}$ Mice Exhibit Over-Connectivity in Cortical and Hippocampal Networks

The significant enrichment of cell adhesion and axonal guidance genes in the downregulated gene set at P5 led us to hypothesize that long-range connectivity might be altered in *Chd8* heterozygous neocortices. To test this hypothesis, we performed rsfMRI to probe functional brain connectivity in mature brain networks. Synchronous fluctuations in blood-oxygen-level dependent (BOLD) signals in different brain regions are used as an indication of them being functionally connected. A regionally unbiased analysis for long-range connectivity changes revealed hotspots for increased connectivity in *Chd8*$^{+/-}$ mice compared with wildtype littermate controls, which included the entorhinal, retrosplenial, auditory cortical and posterior hippocampal areas (*t*-test, $P < 0.05$ FEW cluster-corrected, with cluster-defining threshold $t_{24} > 2.06$, $P < 0.05$; orange areas in Fig. 5A). This analysis suggested that hyperconnected areas were predominantly located on the left side of the brain. A reanalysis of these results without the use of cluster correction revealed the presence of foci with increased connectivity also on the right side, mirroring the effects observed on the left (dark red areas in Fig. 5A). Interhemispheric mapping of rsfMRI connectivity strength in previously characterized rsfMRI network systems of the mouse brain (Sforazzini et al. 2014), revealed increased cortical connectivity in auditory regions ($P < 0.05$, student's *t*-test, uncorrected), although the effect did not survive FDR correction ($q = 0.05$) for multiple comparison across the rsfMRI networks probed. We next used a seed-based approach to specifically probe regions with altered connectivity to these hotspots to reveal the brain networks affected. Most strikingly, this revealed a reciprocal increase in connectivity between ventral hippocampus and auditory cortical regions in *Chd8* mutant mice (*t*-test, $P < 0.05$ FEW cluster-corrected, with cluster-defining threshold $t_{24} > 2.06$, $P < 0.05$; Fig. 5B,C). Seed placement in the auditory cortex revealed increased connectivity of this region with both cingulate and entorhinal cortices (Fig. 5B), whereas a hippocampal seed uncovered strengthened long-range connectivity with somatosensory and visual cortices (Fig 5C).

Previous studies suggested that neurodevelopmental genes show correlated expression patterns in brain areas that are connected (French and Pavlidis 2011). To test if the same applies to our model we harnessed gene expression data contained within the Allen brain atlas to identify genes that are highly expressed in hippocampal and auditory areas. Using expression data from the Allen brain atlas, we determined genes with high relative expression in both the hippocampal CA2 region and auditory areas (Supplementary Fig. S4A, B; Supplementary Table S11; see Methods for details). Enriched genes preferentially clustered into GO term categories relating

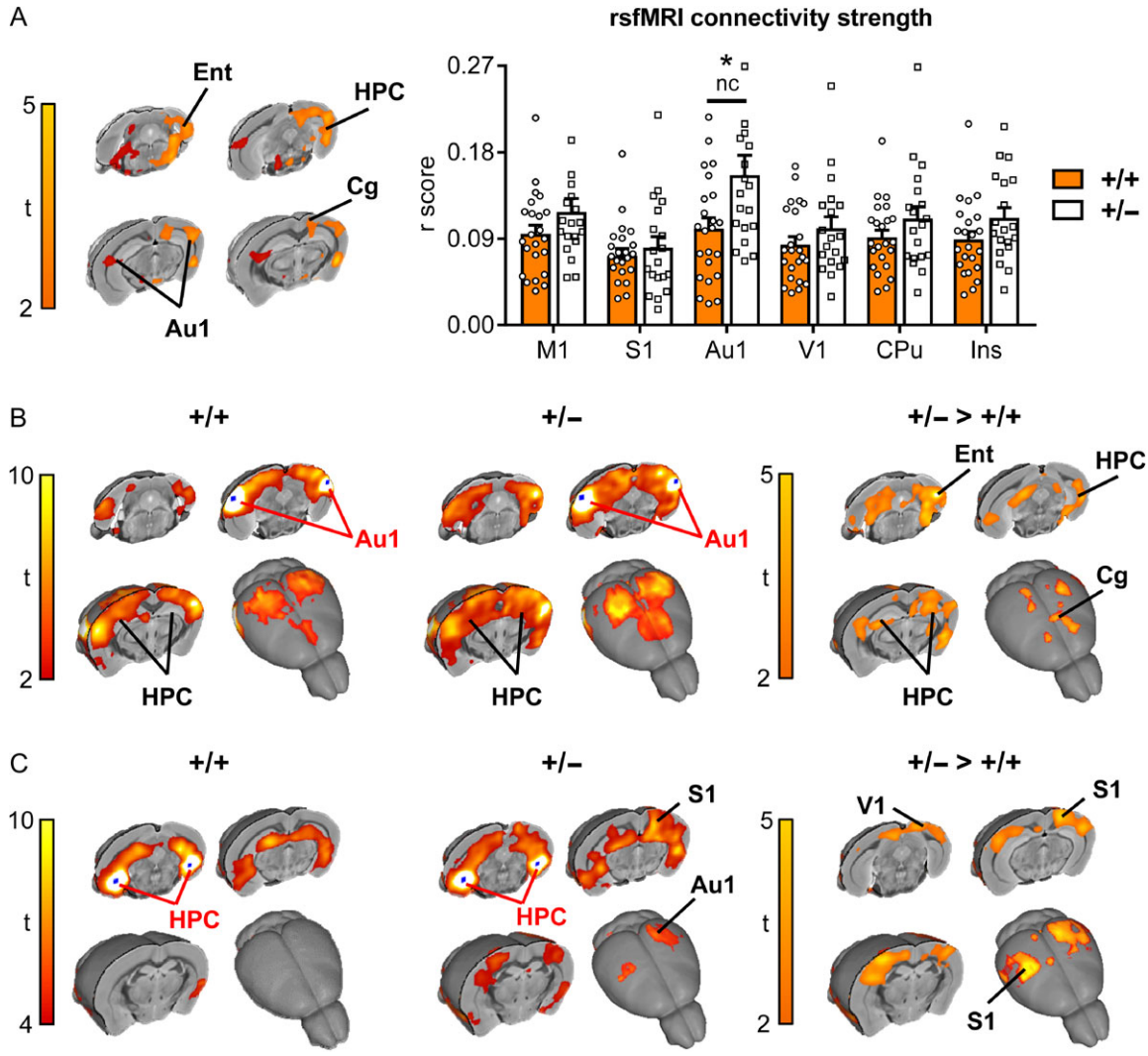

Figure 5. Resting-state functional MRI reveals increased parietohippocampal connectivity in *Chd8*$^{+/-}$ mice. (*A*) Global (long range) connectivity mapping revealed bilateral foci of increased connectivity in posterior cortical and hippocampal regions in *Chd8*$^{+/-}$ mice with respect to control littermates (*Chd8*$^{+/-}$: $n = 19$, *Chd8*$^{+/+}$: $n = 23$). The effect is shown at a threshold $t_{24} > 2.06$, $P < 0.05$ (Fig. 5A). Orange areas indicate regional rsfMRI differences surviving cluster correction ($P = 0.05$). The bar plot on the right displays global connectivity strength quantification (*r* score) in bilateral areas of interest. *$P < 0.05$, nc = not corrected for multiple comparisons. Ent = entorhinal cortex, HPC = hippocampus, Au1 = auditory cortex, Rs = retrosplenial cortex, M1 = motor cortex, S1 = somatosensory cortex, V1 = visual cortex, CPu = caudate putamen. Ins = insular cortex. (*B*) Seed based connectivity mapping obtained using a bilateral auditory seed (Au1) covering foci of increased global rsfMRI connectivity depicted in (*A*). A robust increase in rsfMRI connectivity was observed in hippocampal (HPC), entorhinal (Ent), and cingulate (Cg) regions of *Chd8*$^{+/-}$ mice ($t < 2$, pc = 0.01). (*C*) Seed based connectivity mapping obtained using a bilateral ventro-hippocampal seed (HPC) covering bilateral foci of increased global rsfMRI connectivity in (*A*). A significant increase in rsfMRI connectivity was observed in peri-hippocampal and auditory/parietal (S1 and V1) regions in *Chd8*$^{+/-}$ mice ($t < 2$, pc = 0.01).

to synaptic development and function, axonal structure and neuron projections (Supplementary Table S11). To determine if any of these highly expressed genes are likely contributing to a developing process linked to the functional connectivity phenotype, we compared them with the DEG set from our P5 RNAseq experiment. This analysis revealed several axon guidance and cell adhesion genes that are preferentially expressed in CA2 and auditory areas at adult stages and whose expression is dysregulated at P5 (e.g., *Cdh2, Cdh11, Cdk5r1, Epha4, Fat3, Nrcam, Robo1*; Supplementary Table S11).

Taken together, two independent experimental approaches at different time points identified specific axon guidance and cell adhesion genes, further strengthening our hypothesis that dysregulation of these genes may be important for the functional connectivity phenotype and provides a solid platform for future detailed analyses.

We conclude that early postnatal gene expression changes prefigure abnormal functional connectivity in *Chd8* heterozygous mice. Our findings suggest that abnormalities in specific cortical–hippocampal circuits involved in sensory processing may underlie some of the unique anomalous behaviors observed in *Chd8*$^{+/-}$ mice, and by extension, the neuropsychiatric symptoms in patients with *CHD8* mutations.

Discussion

Here we identify a crucial developmental role for *Chd8* in regulating axon guidance gene expression in the early postnatal period and, for the first time, associate *Chd8* haploinsufficiency with functional over-connectivity of specific brain areas. A recent rsfMRI study involving over 150 male probands with an ASD diagnosis and nearly 200 typically developing individuals

described over-connectivity between sensory cortices and subcortical structures as a central feature in ASD (Cerliani et al. 2015). It will be very important to determine whether these specific functional connectivity abnormalities are present in patients with *CHD8* mutations.

While we cannot at this stage establish a direct causal relationship between transcriptional, connectivity and behavioral phenotypes, our data suggest that functionally altered connectivity of sensory cortical areas in *Chd8* mutant mice underpins behavioral phenotypes. In concordance with previous studies (Katayama et al. 2016; Gompers et al. 2017), our data suggest that moderate expression changes of many genes, rather than severe disruption of few genes, cooperate to give rise to phenotypic changes in *Chd8*$^{+/-}$ mice. A total of 21 axon guidance genes are downregulated in the early postnatal period in our *Chd8*$^{+/-}$ mice (Supplementary Table S6). Therefore, experimental validation of a causal link will be challenging as multiple axon guidance pathways may contribute to the functional connectivity and behavioral phenotypes.

Chd8$^{+/-}$ Mice as a Model for Human *CHD8* Haploinsufficiency Syndrome

CHD8 is one of the highest confidence ASD-associated genes to emerge from recent exome sequencing studies (Neale et al. 2012; Talkowski et al. 2012; O'Roak et al. 2012a; Bernier et al. 2014; Iossifov et al. 2014). We therefore expected *Chd8*$^{+/-}$ mice to present with robust, autism-associated behaviors. *Chd8*$^{+/-}$ mice displayed delayed motor development and distinctive behavioral anomalies that featured a heightened interest in social cues, but surprisingly did not include repetitive and perseverative behaviors or communication deficits.

In agreement with other published studies (Katayama et al. 2016; Gompers et al. 2017; Platt et al. 2017) we did not observe repetitive behaviors in *Chd8*$^{+/-}$ mice. While Katayama et al. reported increased persistence following directional reversal in the T-maze forced alteration test, suggestive of perseverative behaviors, we did not find such evidence in the Morris water maze test. This may be due to the higher complexity of decision making in the Morris water maze compared with the binary choice required by the T-maze. In addition, *Chd8*$^{+/-}$ mice consistently did not show any evidence for perseverative behaviors in the marble burying test (Fig. 2*N*; Gompers et al. 2017; Platt et al. 2017), suggesting that any perseverative behaviors in *Chd8* mutants may be subtle or task-specific. *Chd8*$^{+/-}$ mice show an apparent heightened interest in social cues, indicating that altering the *Chd8* gene dosage during development can impact socially motivated behaviors (Fig. 2*E*). An increased duration of contacts in the social investigation test was also seen in two other published behavioral analyses of *Chd8* heterozygous mouse models (Katayama et al. 2016; Platt et al. 2017). Katayama et al. additionally described a reduced duration of active social contacts in *Chd8* mutants, although all test groups showed evidence for high levels of anxiety, a known behavioral confound. Katayama et al. (2016) and Platt et al. (2017) further reported normal sociability but minor deficits in social novelty in the 3-chamber social approach task in *Chd8*$^{+/-}$ mice.

Despite not observing typical ASD-like behaviors, we did detect a delay in early motor development in *Chd8*$^{+/-}$ mice (Fig. 2*A*,*B*). There is a growing body of evidence suggesting that delayed motor milestones in toddlers predate and predict the emergence and severity of language deficits in later life (Bedford et al. 2016; Chinello et al. 2016). Of note, the only available longitudinal case reports in the literature also describe early motor delay in both patients with *CHD8* haploinsufficiency (Merner et al. 2016; Stolerman et al. 2016).

A key characteristic of autism is restricted behaviors or interests, which often manifest as hyper- or hyporeactivity to sensory input or unusual interest in sensory stimuli, for example, excessive smelling or touching of objects (Constantino and Charman 2016). One may speculate that the excessive smelling of social cues and the increased duration of social contacts observed in our *Chd8*$^{+/-}$ mice may be indicative of behavioral abnormalities in these domains.

Dysregulation of the Cortical Transcriptome in *Chd8* Heterozygous Mice

Gene expression analysis showed little evidence for transcriptional dysregulation at midembryonic stages, but revealed disruption of key developmental processes involved in establishing brain connectivity in the early postnatal neocortex. These data are in agreement with a recent study where Gompers and colleagues only found a handful of genes differentially expressed in bulk forebrain at E12.5 and E14.5, while detecting subtle, more widespread changes perinatally (E17.5: 89 DEGs, P0: 35 DEGs; FDR < 0.05) and more pronounced dysregulation at adult stages (295 DEGs; FDR < 0.05) (Gompers et al. 2017).

Many of the transcripts that were dysregulated in the early postnatal period are themselves ASD-associated genes and were predominantly downregulated. Our gene expression studies therefore provided strong evidence that a variety of genes, pathways and developmental processes implicated in ASD might be dysregulated by *Chd8* haploinsufficiency.

An expanding number of ASD risk genes have roles in axon guidance, synapse development and plasticity (Bourgeron 2015). We detected significant enrichment of genes in these functional categories in our downregulated gene set, including the major Slit protein receptors *Robo1* and *Robo2*, *EhpA4* and 5, and cell adhesion molecules such as *L1CAM* and *Cdh2, 5, 8,* and *11* (Supplementary Tables S3 and S6). Similarly, Gompers et al. found enrichment for axon growth and guidance factors amongst downregulated genes in their M3 module (Gompers et al. 2017). Moreover, Sugathan et al. showed enrichment for genes associated with the GO terms "cell adhesion," "axon guidance," and "neuron differentiation" amongst downregulated genes in *CHD8*- deficient human iPSC-derived neural progenitors. This suggests that these important developmental gene sets are regulated by CHD8 in both mouse and human cells (Sugathan et al. 2014).

In sum, our data identify early postnatal development as a key stage at which transcriptional changes caused by *Chd8* heterozygosity may precipitate ASD-related phenotypes. They further indicate that *Chd8* heterozygosity defines a transcriptional program characterized by diminished expression of key neurodevelopmental regulators that are predicted to affect cellular functions essential for the appropriate wiring of the brain.

Increased Functional Connectivity in Sensory Networks

Significantly, functional connectivity was altered in the adult brain of *Chd8*$^{+/-}$ mice. Our rsfMRI analysis found evidence for over-connectivity between sensory regions in the neocortex and limbic cortical regions. Most notably, the auditory cortex showed a global increase in functional connectivity that involved connections to other cortical areas and reciprocal strengthening of connectivity to the ventral hippocampus. It seems likely that altered connectivity is the consequence of

some of the disrupted brain wiring pathways uncovered by our RNA-seq experiments. Encouragingly, the expression of several axon guidance and cell adhesion genes, which are dysregulated at P5, is enriched in hippocampus and auditory cortex (Supplementary Table S11); nevertheless, this hypothesis will require further in-depth scrutiny. More importantly, it will be critical to investigate whether these connectivity changes are pertinent to any of the behavioral anomalies in *Chd8* heterozygous mice or the ASD phenotype in patients with *CHD8* haploinsufficiency. The over-connectivity in networks involving the auditory cortex and the hippocampus is intriguing. Auditory processing deficits in ASD are well documented and range from a lack of lateralization to a general delay in network maturation (Bruneau et al. 1992; Edgar et al. 2015), although the functional behavioral consequences of these deficits are not clear. Furthermore, over-responsivity to sensory stimuli is frequently observed in ASD patients, can affect all sensory modalities and appears to be positively correlated with the severity of autistic traits (reviewed in Tavassoli et al. 2014; Sinclair et al. 2017). Although a definitive causal relationship is difficult to establish, it has been hypothesized that sensory over-responsivity may trigger compensatory and avoidance behaviors that promote the emergence of core behavioral autism traits (Marco et al. 2011). In support, tactile hypersensitivity during critical developmental periods has been shown to underlie anxiety and social deficits in a number of genetic ASD mouse models (Orefice et al. 2016). Whether this would be equally the case for other sensory modalities and a general mechanistic feature in the behavioral aetiology of ASD remains an open question.

Supplementary Material

Supplementary material is available at *Cerebral Cortex* online.

Funding

We acknowledge research grants from the Medical Research Council (MR/K022377/1 to M.A.B. and C.F.), Simons Foundation (SFARI #344763 to M.A.B.; SFARI #400101 to A.G.), Ontario Brain Institute's POND program (J.P.L.), and BBSRC (BB/K008668/1 to P.F.W.). S.H. and R.E. were supported by the King's Bioscience Institute and the Guy's and St Thomas' Charity Prize PhD Program in Biomedical and Translational Science. A.G. was supported by a 2017 NARSAD Independent Investigator Grant from the Brain and Behavior Research Foundation.

Notes

We thank John Whittingham, Alex Donovan and BSU staff for technical assistance and Chris Healy for μCT scans. We acknowledge the High-Throughput Genomics Group at the Wellcome Trust Center for Human Genetics (funded by Wellcome Trust grant reference 090532/Z/09/Z) for the generation of the RNA sequencing data and Drs. Brian Nieman and Leigh Spencer Noakes for their MRI sequences. We also thank the Allen Institute for Brain Science for providing gene expression data used in this study (© 2004 Allen Institute for Brain Science. Allen Mouse Brain Atlas. Available from: http://mouse.brain-map.org). *Conflict of Interest*: none declared.

References

Andrews S. 2010. FASTQC. A quality control tool for high throughput sequence data. Available from: http://www.bioinformatics.babraham.ac.uk/projects/fastqc/

APA. 2013. Diagnostic and statistical manual of mental disorders. Arlington, VA: American Psychiatric Publishing.

Avants BB, Tustison NJ, Song G, Gee JC. 2009. ANTS: Advanced Open-Source Normalization Tools for Neuroanatomy. Penn Image Computing and Science Laboratory.

Barnard RA, Pomaville MB, O'Roak BJ. 2015. Mutations and modeling of the chromatin remodeler chd8 define an emerging autism etiology. Front Neurosci. 9:477.

Bedford R, Pickles A, Lord C. 2016. Early gross motor skills predict the subsequent development of language in children with autism spectrum disorder. Autism Res. 9(9):993–1001.

Belmonte MK, Allen G, Beckel-Mitchener A, Boulanger LM, Carper RA, Webb SJ. 2004. Autism and abnormal development of brain connectivity. J Neurosci Nurs. 24(42):9228–9231.

Bernier R, Golzio C, Xiong B, Stessman HA, Coe BP, Penn O, Witherspoon K, Gerdts J, Baker C, Vulto-van Silfhout AT, et al. 2014. Disruptive chd8 mutations define a subtype of autism early in development. Cell. 158(2):263–276.

Blatt GJ. 2012. The neuropathology of autism. Scientifica (Cairo). 2012:703675.

Bourgeron T. 2015. From the genetic architecture to synaptic plasticity in autism spectrum disorder. Nat Rev Neurosci. 16 (9):551–563.

Bruneau N, Dourneau MC, Garreau B, Pourcelot L, Lelord G. 1992. Blood flow response to auditory stimulations in normal, mentally retarded, and autistic children: a preliminary transcranial doppler ultrasonographic study of the middle cerebral arteries. Biol Psychiatry. 32(8):691–699.

Cao R, Zhang Y. 2004. Suz12 is required for both the histone methyltransferase activity and the silencing function of the eed-ezh2 complex. Mol Cell. 15(1):57–67.

Cerliani L, Mennes M, Thomas RM, Di Martino A, Thioux M, Keysers C. 2015. Increased functional connectivity between subcortical and cortical resting-state networks in autism spectrum disorder. JAMA Psychiatry. 72(8):767–777.

Chakravarty MM, Steadman P, van Eede MC, Calcott RD, Gu V, Shaw P, Raznahan A, Collins DL, Lerch JP. 2013. Performing label-fusion-based segmentation using multiple automatically generated templates. Human Brain Mapping. 34(10): 2635–2654.

Chen EY, Tan CM, Kou Y, Duan Q, Wang Z, Meirelles GV, Clark NR, Ma'ayan A. 2013. Enrichr: interactive and collaborative html5 gene list enrichment analysis tool. BMC Bioinf. 14:128.

Cherkassky VL, Kana RK, Keller TA, Just MA. 2006. Functional connectivity in a baseline resting-state network in autism. NeuroReport. 17(16):1687–1690.

Chinello A, Di Gangi V, Valenza E. 2016. Persistent primary reflexes affect motor acts: potential implications for autism spectrum disorder. Research in Developmental Disabilities.

Constantino JN, Charman T. 2016. Diagnosis of autism spectrum disorder: reconciling the syndrome, its diverse origins, and variation in expression. Lancet Neurol. 15(3):279–291.

Cotney J, Muhle RA, Sanders SJ, Liu L, Willsey AJ, Niu W, Liu W, Klei L, Lei J, Yin J, et al. 2015. The autism-associated chromatin modifier chd8 regulates other autism risk genes during human neurodevelopment. Nat Commun. 6:6404.

Croen LA, Zerbo O, Qian Y, Massolo ML, Rich S, Sidney S, Kripke C. 2015. The health status of adults on the autism spectrum. Autism. 19(7):814–823.

Di Martino A, Yan CG, Li Q, Denio E, Castellanos FX, Alaerts K, Anderson JS, Assaf M, Bookheimer SY, Dapretto M, et al. 2014. The autism brain imaging data exchange: towards a large-scale evaluation of the intrinsic brain architecture in autism. Mol Psychiatry. 19(6):659–667.

Donovan AP, Basson MA. 2017. The neuroanatomy of autism—a developmental perspective. J Anat. 230(1):4–15.

Durak O, Gao F, Kaeser-Woo YJ, Rueda R, Martorell AJ, Nott A, Liu CY, Watson LA, Tsai LH. 2016. Chd8 mediates cortical neurogenesis via transcriptional regulation of cell cycle and wnt signaling. Nat Neurosci. 19(11):1477.

Ecker C. 2016. The neuroanatomy of autism spectrum disorder: an overview of structural neuroimaging findings and their translatability to the clinical setting. Autism. 21(1): 18–208.

Eden E, Navon R, Steinfeld I, Lipson D, Yakhini Z. 2009. Gorilla: a tool for discovery and visualization of enriched go terms in ranked gene lists. BMC Bioinf. 10:48.

Edgar JC, Fisk Iv CL, Berman JI, Chudnovskaya D, Liu S, Pandey J, Herrington JD, Port RG, Schultz RT, Roberts TP. 2015. Auditory encoding abnormalities in children with autism spectrum disorder suggest delayed development of auditory cortex. Molecular Autism. 6:69.

Ferrari L, Turrini G, Crestan V, Bertani S, Cristofori P, Bifone A, Gozzi A. 2012. A robust experimental protocol for pharmacological fMRI in rats and mice. J Neurosci Methods. 204(1): 9–18.

French L, Pavlidis P. 2011. Relationships between gene expression and brain wiring in the adult rodent brain. PLoS Comput Biol. 7(1):e1001049.

Friedel M, van Eede MC, Pipitone J, Chakravarty MM, Lerch JP. 2014. Pydpiper: a flexible toolkit for constructing novel registration pipelines. Front Neuroinform. 8:67.

Gompers AL, Su-Feher L, Ellegood J, Copping NA, Riyadh MA, Stradleigh TW, Pride MC, Schaffler MD, Wade AA, Catta-Preta R, et al. 2017. Germline chd8 haploinsufficiency alters brain development in mouse. Nat Neurosci. 20(8):1062.

Hill CA, Sussan TE, Reeves RH, Richtsmeier JT. 2009. Complex contributions of ets2 to craniofacial and thymus phenotypes of trisomic "down syndrome" mice. Am J Med Genet A. 149A (10):2158–2165.

Huang DW, Sherman BT, Lempicki RA. 2009. Systematic and integrative analysis of large gene lists using david bioinformatics resources. Nat Protoc. 4(1):44–57.

Iossifov I, O'Roak BJ, Sanders SJ, Ronemus M, Krumm N, Levy D, Stessman HA, Witherspoon KT, Vives L, Patterson KE, et al. 2014. The contribution of de novo coding mutations to autism spectrum disorder. Nature. 515(7526):216–221.

Jeste SS, Tuchman R. 2015. Autism spectrum disorder and epilepsy: two sides of the same coin? J Child Neurol. 30(14): 1963–1971.

Just MA, Cherkassky VL, Keller TA, Minshew NJ. 2004. Cortical activation and synchronization during sentence comprehension in high-functioning autism: evidence of underconnectivity. Brain. 127(Pt 8):1811–1821.

Katayama Y, Nishiyama M, Shoji H, Ohkawa Y, Kawamura A, Sato T, Suyama M, Takumi T, Miyakawa T, Nakayama KI. 2016. Chd8 haploinsufficiency results in autistic-like phenotypes in mice. Nature. 537(7622):675–679.

Kim D, Pertea G, Trapnell C, Pimentel H, Kelley R, Salzberg SL. 2013. Tophat2: accurate alignment of transcriptomes in the presence of insertions, deletions and gene fusions. Genome Biol. 14(4):R36.

Krueger F. 2012. Trim Galore! Available from: http://www.bioinformatics.babraham.ac.uk/projects/trim_galore/

Lein ES, Hawrylycz MJ, Ao N, Ayres M, Bensinger A, Bernard A, Boe AF, Boguski MS, Brockway KS, Byrnes EJ, et al. 2007. Genome-wide atlas of gene expression in the adult mouse brain. Nature. 445(7124):168–176.

Lewandoski M, Martin GR. 1997. Cre-mediated chromosome loss in mice. Nat Genet. 17(2):223–225.

Liao Y, Smyth GK, Shi W. 2014. Featurecounts: an efficient general purpose program for assigning sequence reads to genomic features. Bioinformatics. 30(7):923–930.

Liska A, Bertero A, Gomolka R, Sabbioni M, Galbusera A, Barsotti N, Panzeri S, Scattoni ML, Pasqualetti M, Gozzi A. 2017. Homozygous loss of autism-risk gene cntnap2 results in reduced local and long-range prefrontal functional connectivity. Cereb Cortex. 10:1–13.

Liska A, Galbusera A, Schwarz AJ, Gozzi A. 2015. Functional connectivity hubs of the mouse brain. NeuroImage. 115: 281–291.

Liska A, Gozzi A. 2016. Can mouse imaging studies bring order to autism connectivity chaos? Front Neurosci. 10:484.

Liu X, Zhu XH, Zhang Y, Chen W. 2011. Neural origin of spontaneous hemodynamic fluctuations in rats under burst-suppression anesthesia condition. Cereb Cortex. 21(2): 374–384.

Love MI, Huber W, Anders S. 2014. Moderated estimation of fold change and dispersion for rna-seq data with deseq2. Genome Biol. 15(12):550.

Marco EJ, Hinkley LB, Hill SS, Nagarajan SS. 2011. Sensory processing in autism: a review of neurophysiologic findings. Pediatr Res. 69(5 Pt 2):48R–54R.

Merner N, Forgeot d'Arc B, Bell SC, Maussion G, Peng H, Gauthier J, Crapper L, Hamdan FF, Michaud JL, Mottron L, et al. 2016. A de novo frameshift mutation in chromodomain helicase DNA-binding domain 8 (chd8): a case report and literature review. Am J Med Genet A. 170(5):1225–1235.

Neale BM, Kou Y, Liu L, Ma'ayan A, Samocha KE, Sabo A, Lin CF, Stevens C, Wang LS, Makarov V, et al. 2012. Patterns and rates of exonic de novo mutations in autism spectrum disorders. Nature. 485(7397):242–245.

Ng L, Bernard A, Lau C, Overly CC, Dong HW, Kuan C, Pathak S, Sunkin SM, Dang C, Bohland JW, et al. 2009. An anatomic gene expression atlas of the adult mouse brain. Nat Neurosci. 12(3):356–362.

Orefice LL, Zimmerman AL, Chirila AM, Sleboda SJ, Head JP, Ginty DD. 2016. Peripheral mechanosensory neuron dysfunction underlies tactile and behavioral deficits in mouse models of asds. Cell. 166(2):299–313.

O'Roak BJ, Stessman HA, Boyle EA, Witherspoon KT, Martin B, Lee C, Vives L, Baker C, Hiatt JB, Nickerson DA, et al. 2014. Recurrent de novo mutations implicate novel genes underlying simplex autism risk. Nat Commun. 5:5595.

O'Roak BJ, Vives L, Fu W, Egertson JD, Stanaway IB, Phelps IG, Carvill G, Kumar A, Lee C, Ankenman K, et al. 2012a. Multiplex targeted sequencing identifies recurrently mutated genes in autism spectrum disorders. Science. 338 (6114):1619–1622.

O'Roak BJ, Vives L, Girirajan S, Karakoc E, Krumm N, Coe BP, Levy R, Ko A, Lee C, Smith JD, et al. 2012b. Sporadic autism exomes reveal a highly interconnected protein network of de novo mutations. Nature. 485(7397):246–250.

Picci G, Gotts SJ, Scherf KS. 2016. A theoretical rut: revisiting and critically evaluating the generalized under/over-connectivity hypothesis of autism. Dev Sci. 19(4):524–549.

Platt RJ, Zhou Y, Slaymaker IM, Shetty AS, Weisbach NR, Kim JA, Sharma J, Desai M, Sood S, Kempton HR, et al. 2017. Chd8 mutation leads to autistic-like behaviors and impaired striatal circuits. Cell Rep. 19(2):335–350.

Scott-Van Zeeland AA, Abrahams BS, Alvarez-Retuerto AI, Sonnenblick LI, Rudie JD, Ghahremani D, Mumford JA,

Poldrack RA, Dapretto M, Geschwind DH, et al. 2010. Altered functional connectivity in frontal lobe circuits is associated with variation in the autism risk gene cntnap2. Sci Transl Med. 2(56):56ra80.

Sforazzini F, Bertero A, Dodero L, David G, Galbusera A, Scattoni ML, Pasqualetti M, Gozzi A. 2016. Altered functional connectivity networks in acallosal and socially impaired btbr mice. Brain Struct Funct. 221(2):941–954.

Sforazzini F, Schwarz AJ, Galbusera A, Bifone A, Gozzi A. 2014. Distributed bold and cbv-weighted resting-state networks in the mouse brain. NeuroImage. 87:403–415.

Sinclair D, Oranje B, Razak KA, Siegel SJ, Schmid S. 2017. Sensory processing in autism spectrum disorders and fragile x syndrome-from the clinic to animal models. Neurosci Biobehav Rev. 76(Pt B):235–253.

Steffey MA, Brosnan RJ, Steffey EP. 2003. Assessment of halothane and sevoflurane anesthesia in spontaneously breathing rats. Am J Vet Res. 64(4):470–474.

Stessman HA, Xiong B, Coe BP, Wang T, Hoekzema K, Fenckova M, Kvarnung M, Gerdts J, Trinh S, Cosemans N, et al. 2017. Targeted sequencing identifies 91 neurodevelopmental-disorder risk genes with autism and developmental-disability biases. Nat Genet. 49(4):515–526.

Stolerman ES, Smith B, Chaubey A, Jones JR. 2016. Chd8 intragenic deletion associated with autism spectrum disorder. Eur J Med Genet. 59(4):189–194.

Sugathan A, Biagioli M, Golzio C, Erdin S, Blumenthal I, Manavalan P, Ragavendran A, Brand H, Lucente D, Miles J, et al. 2014. Chd8 regulates neurodevelopmental pathways associated with autism spectrum disorder in neural progenitors. Proc Natl Acad Sci USA. 111(42):E4468–E4477.

Talkowski ME, Rosenfeld JA, Blumenthal I, Pillalamarri V, Chiang C, Heilbut A, Ernst C, Hanscom C, Rossin E, Lindgren AM, et al. 2012. Sequencing chromosomal abnormalities reveals neurodevelopmental loci that confer risk across diagnostic boundaries. Cell. 149(3):525–537.

Tavassoli T, Miller LJ, Schoen SA, Nielsen DM, Baron-Cohen S. 2014. Sensory over-responsivity in adults with autism spectrum conditions. Autism. 18(4):428–432.

Thompson BA, Tremblay V, Lin G, Bochar DA. 2008. Chd8 is an atp-dependent chromatin remodeling factor that regulates beta-catenin target genes. Mol Cell Biol. 28(12): 3894–3904.

Truett GE, Heeger P, Mynatt RL, Truett AA, Walker JA, Warman ML. 2000. Preparation of pcr-quality mouse genomic DNA with hot sodium hydroxide and tris (hotshot). Biotechniques. 29(1):52–54.

Whittaker DE, Riegman KL, Kasah S, Mohan C, Yu T, Sala BP, Hebaishi H, Caruso A, Marques AC, Michetti C, et al. 2017a. The chromatin remodeling factor CHD7 controls cerebellar development by regulating reelin expression. J Clin Invest. 127:874–887.

Whittaker DE, Kasah S, Donovan APA, Ellegood J, Riegman KLH, Volk HA, McGonnell I, Lerch JP, Basson MA. 2017b. Distinct cerebellar foliation anomalies in a chd7 haploinsufficient mouse model of charge syndrome. Am J Med Genet C Semin Med Genet. 175(4). 10.1002/ajmg.c.31595.

Yuan CC, Zhao X, Florens L, Swanson SK, Washburn MP, Hernandez N. 2007. Chd8 associates with human staf and contributes to efficient u6 RNA polymerase iii transcription. Mol Cell Biol. 27(24):8729–8738.

Zhan Y, Paolicelli RC, Sforazzini F, Weinhard L, Bolasco G, Pagani F, Vyssotski AL, Bifone A, Gozzi A, Ragozzino D, et al. 2014. Deficient neuron-microglia signaling results in impaired functional brain connectivity and social behavior. Nat Neurosci. 17(3):400–406.